



HAL
open science

Cavity-type hypersonic phononic crystals

A. Sato, Yan Pennec, T. Yanagishita, H. Masuda, W. Knoll, Bahram Djafari-Rouhani, G. Fytas

► **To cite this version:**

A. Sato, Yan Pennec, T. Yanagishita, H. Masuda, W. Knoll, et al.. Cavity-type hypersonic phononic crystals. *New Journal of Physics*, 2012, 14, pp.113032. 10.1088/1367-2630/14/11/113032 . hal-00787468

HAL Id: hal-00787468

<https://hal.science/hal-00787468>

Submitted on 12 Jul 2022

HAL is a multi-disciplinary open access archive for the deposit and dissemination of scientific research documents, whether they are published or not. The documents may come from teaching and research institutions in France or abroad, or from public or private research centers.

L'archive ouverte pluridisciplinaire **HAL**, est destinée au dépôt et à la diffusion de documents scientifiques de niveau recherche, publiés ou non, émanant des établissements d'enseignement et de recherche français ou étrangers, des laboratoires publics ou privés.



Distributed under a Creative Commons Attribution - ShareAlike 4.0 International License

PAPER • OPEN ACCESS

Cavity-type hypersonic phononic crystals

To cite this article: A Sato *et al* 2012 *New J. Phys.* **14** 113032

View the [article online](#) for updates and enhancements.

You may also like

- [Large gain quantum-limited qubit measurement using a two-mode nonlinear cavity](#)
S Khan, R Vijay, I Siddiqi et al.
- [Enhanced electrochemical performance of hierarchical porous carbon/polyaniline composite for supercapacitor applications](#)
Sangeeta Rawal, U K Mandal, Ashwani Kumar et al.
- [Fabrication and optical property of metal nanowire arrays embedded in anodic porous alumina membrane](#)
Kouichi Takase, Tomohiro Shimizu, Kosuke Sugawa et al.

Cavity-type hypersonic phononic crystals

A Sato^{1,6}, Y Pennec², T Yanagishita³, H Masuda³, W Knoll⁴,
B Djafari-Rouhani^{2,7} and G Fytas^{1,5,7}

¹ Max Planck Institute for Polymer Research, Ackermannweg 10, 55128 Mainz, Germany

² Institut d'Electronique de Microélectronique et de Nanotechnologie, UMR CNRS 8520, Université de Lille 1, Sciences et Technologies, 59652 Villeneuve d'Ascq, France

³ Department of Applied Chemistry, School of Engineering, Tokyo Metropolitan University, 1-1 Minamiosawa, Hachioji, Tokyo 192-0397, Japan

⁴ Austrian Research Centers GmbH, Donau-City-Street 1, 1220 Vienna, Austria

⁵ Department of Materials Science and FORTH, 71110 Heraklion, Greece

E-mail: bahram.djafari-rouhani@univ-lille1.fr and fytas@mpip-mainz.mpg.de

New Journal of Physics **14** (2012) 113032 (13pp)


Received 9 August 2012

Published 22 November 2012

Online at <http://www.njp.org/>

doi:10.1088/1367-2630/14/11/113032

Abstract. We report on the engineering of the phonon dispersion diagram in monodomain anodic porous alumina (APA) films through the porosity and physical state of the material residing in the nanopores. Lattice symmetry and inclusion materials are theoretically identified to be the main factors which control the hypersonic acoustic wave propagation. This involves the interaction between the longitudinal and the transverse modes in the effective medium and a flat band characteristic of the material residing in the cavities. Air and filled nanopores, therefore, display markedly different dispersion relations and the inclusion materials lead to a locally resonant structural behavior uniquely determining their properties under confinement. APA films emerge as a new platform to investigate the rich acoustic phenomena of structured composite matter.

 Online supplementary data available from stacks.iop.org/NJP/14/113032/mmedia

⁶ Present address: Laboratoire d'Optique Biomédicale, Ecole Polytechnique Fédérale de Lausanne, CH-1015 Lausanne, Switzerland

⁷ Authors to whom any correspondence should be addressed.



Content from this work may be used under the terms of the [Creative Commons Attribution-NonCommercial-ShareAlike 3.0 licence](http://creativecommons.org/licenses/by-nc-sa/3.0/). Any further distribution of this work must maintain attribution to the author(s) and the title of the work, journal citation and DOI.

Contents

1. Introduction	2
2. Experiment	3
2.1. Anodic porous alumina	3
2.2. Brillouin light scattering spectroscopy	3
3. Phonon dispersion diagrams	4
3.1. APA with air cylinders	4
3.2. APA with liquid poly-ethylene oxide cylinders	7
3.3. APA with solid cylinders	10
4. Conclusions	11
Acknowledgments	12
References	12

1. Introduction

Phononics is a growing new area of scientific interest [1, 2] that includes phononic crystals [3, 4] and acoustic metamaterials [5]. In the former, the elastic moduli and mass densities of the constituents are periodically modulated in space. In the latter, the local resonances and subwavelength behavior of the structures are involved and the periodicity is not a prerequisite of the system. Therefore, phenomena such as hybridization gaps [6] can tolerate some disorders [7–9]. Both topics have revealed a great number of new functions such as negative refraction [10, 11], phonon metamaterials [12], acoustic cloaking [13] and acoustic diodes [14, 15]. Most realizable phononic structures lie in the sonic and ultrasonic frequency region requiring a structure periodicity, respectively, in the millimeter to micrometer range [5, 16, 17]. Progress in phononic crystals, supported by recent advances in nanofabrication techniques, led to functional hypersonic (GHz range) phononic structures [7, 18–26]. Recent years have witnessed a growing interest in hypersonic phononics due to new ways of manipulation of the phonon propagation in periodic structures and potential technological applications such as dual bandgap structures [27], acousto-optical devices [28, 29] with phonon–photon interaction in a cavity, heat management [1, 30] and elastic mirrors [31]. However, a detailed understanding of phonon propagation in the hypersonic regime remains a key issue for phonon band structure engineering at high frequencies. It is not only the search for a large complete bandgap of interest but also the effect of periodicity on phonon propagation out of the bandgap region that is important for several applications. However, the ‘champion’ phononic structure for a given contrast in the mechanical impedance of the material components has to be defined. Although pillar-type phononic crystals possess large bandgaps from a theoretical point of view, such structures are more difficult to fabricate due to the neck formation [32] at the nanoscale. Hence, we first address the dispersion relations in cavity-type hypersonic phononic crystals exemplified by two-dimensional (2D) anodic porous alumina (APA).

APA contains hexagonal arrays of aligned nanopores oriented normal to the film surface. Since photonic bandgaps have been realized in APA in the visible and infrared regions [33, 34], these structures can also provide a feasible platform to develop dual bandgap crystals realizing acousto-optical interactions and allow for the generation of stimulated backscattering [35]. Investigations on hypersonic phononic properties of APA were initiated recently [36–38].

However, the lack of long-range periodicity and inaccessibility to an appropriate range of spacing (200–500 nm) have restricted the experiment to the long phonon wavelengths and rendered a comparison to the theory incomplete.

In this work, we verified the complete phonon dispersion relation $\omega(\mathbf{q})$ along two high-symmetry directions in APA with both air and filled cylinders using Brillouin light scattering (BLS) [37] and the finite difference time domain (FDTD) method for band structure calculations [17]. The utility of the present monodomain APA helped unveil the strong modification of the phonon propagation upon filling the nanopores not anticipated from the study of polydomain APA [36]. The experimental phononic band diagram consists of three modes (1–3 towards increasing frequency) with different dispersions for monodomain APAs, whereas polydomain APAs display only mode (1) [36]. Filling the nanopores induces a strong and direction-independent bending in the dispersion of mode (1). Based on the FDTD calculation of the band structure, the interaction between the first (i) and second (ii) propagation band in the case of air cylinders leads to a characteristic bending of the former band. In contrast, APA with liquid or solid cylinders shows a locally resonant structural behavior reported earlier for a sonic crystal [5]. APA holds promise of a facile platform to manipulate the flow of elastic energy by means of adverse filling materials with a possible impact on their physical state due to confinement and interactions with the nanopore surfaces.

2. Experiment

2.1. Anodic porous alumina

We fabricated 2D-hypersonic phononic crystals based on self-ordered APA by the pretexturing anodization process [33, 39], which yields almost defect-free long-ranged-ordered nanopore arrays. The pretexturing anodization involves the introduction of hexagonally arranged concaves to the electropolished Al surface. This molding process essentially fabricates the initiation point and allows for continuous growth of the ordered nanopore arrays. Our samples contain hexagonal arrays of air cylinders in the APA matrix with a thickness of $40\ \mu\text{m}$ and a lattice constant of $a = 200\ \text{nm}$. We investigated two monodomain APA films with diameters of 100 and 150 nm and corresponding porosities ($p = \pi d^2 / (2\sqrt{3}a^2)$), 23 and 51%. The SEM images of figures 1(a) and (b) clearly demonstrate the coherent structure of the two films. In addition, we infiltrated the APA films with poly(ethylene oxide) (PEO; Fulka, $M_n = 20\ \text{kg mol}^{-1}$) at $80\ ^\circ\text{C}$, well above the melting temperature ($T_m \sim 65\ ^\circ\text{C}$).

2.2. Brillouin light scattering spectroscopy

The phononic dispersion relations were measured by BLS for the two APA with air and PEO cylinders with PEO being either in the liquid ($70\ ^\circ\text{C}$) or in the semi-crystalline ($20\ ^\circ\text{C}$) state. For the given experimental conditions, the scattering wave vector \mathbf{q} lies in the ΓX and ΓJ directions of the hexagonal lattice, and its amplitude $q = (4\pi/\lambda)\sin(\theta/2)$ (normal to the nanopores) depends on the scattering angle θ and the wavelength of the incident laser light λ ($= 532\ \text{nm}$) (figure 1(c)). The direction of \mathbf{q} in the Brillouin zone (BZ) is changed by rotating the samples by 90° about the normal to the film. The polarization of the incident light was vertical (V), while the polarization of the scattered light was chosen either vertical (V) or horizontal (H) relative to the scattering plane defined by \mathbf{k}_i and \mathbf{k}_s , which are the wave vectors of the incident and

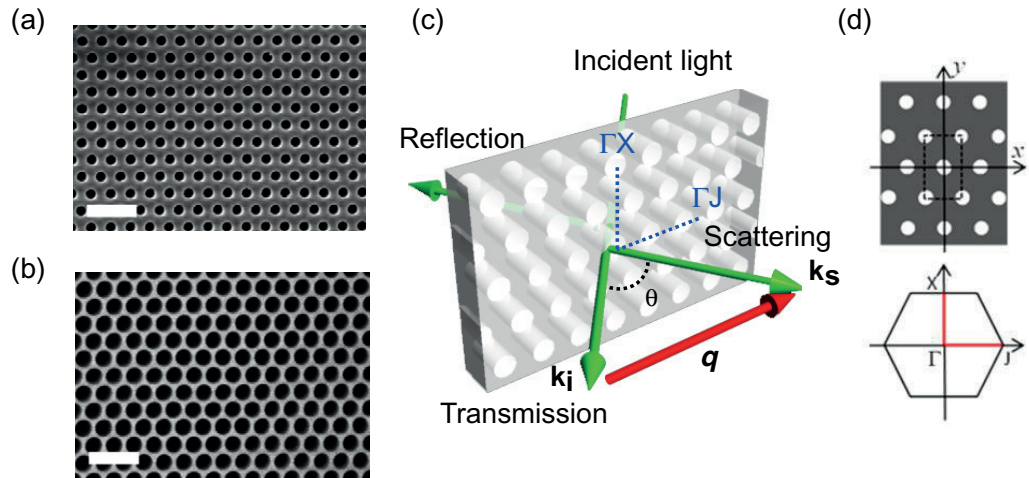


Figure 1. Scanning electron microscope (SEM) images of APA (lattice constant $a = 200$ nm) and phonon propagation direction parallel to the film (thickness $40 \mu\text{m}$) with different pore diameter, d , and porosity, p . (a) $p = 0.23$ with $d = 100$ nm and (b) $p = 0.51$ with $d = 150$ nm. Scale bars represent 500 nm. (c) The phonon wave vector q at a scattering angle θ is defined by the wave vectors k_i and k_s of the transmitted and scattered light. The phonon propagation direction is controlled by rotating the sample about the normal to the film. (d) Real space representation of the phononic crystal of hexagonal symmetry in the (x, y) -plane and the associated BZ in the reciprocal space. ΓJ and ΓX represent the main directions of the irreducible BZ.

scattered light (figure 1(c)). Polarized (VV) BLS probes predominantly longitudinal modes, while depolarized (VH) BLS records phonons with transverse polarization; transverse modes were recorded for the 23% porosity APA with air cylinders (see below).

Figures 2(a) and (b) compare VV BLS spectra of the monodomain APA with air cylinders at ambient temperature along two symmetry directions, ΓJ and ΓX ; these are depicted in real and reciprocal space in figure 1(d). The displayed BLS spectra were recorded at $q = 0.0181$ and 0.0193 nm^{-1} near the edge of the BZ along ΓX (at $q_X = 0.0181 \text{ nm}^{-1}$) and ΓJ (at $q_J = 0.021 \text{ nm}^{-1}$). As these periodic structures show photonic bandgaps in the green region [33], the intensity of the transmitted light beam is reduced, thus causing a relatively large noise in the spectra. Nevertheless, different spectra are observed along ΓJ and ΓX for both porosities, in contrast to the polydomain APA [36] for which only the porosity matters. Filling the nanopores with PEO further leads to strong spectral changes (see figure 4). The obtained experimental and computed phonon dispersion relations for the three cases are separately presented in the next section.

3. Phonon dispersion diagrams

3.1. APA with air cylinders

BLS spectra display a peak associated with a longitudinal phonon (1) according to its linear dispersion at low wave vectors, q 's as seen in the dispersion relation plots in figures 3(a)

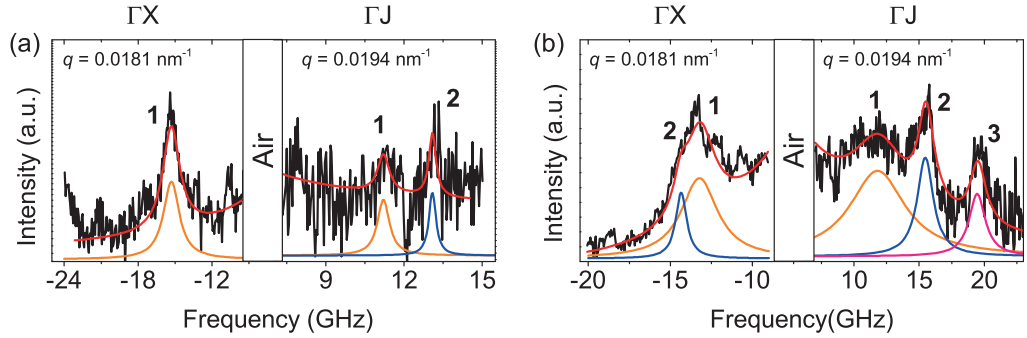


Figure 2. Polarized BLS spectra of APA of air cylinders with two porosities, (a) $p = 0.23$ (lattice constant $a = 200$ nm and diameter $d = 100$ nm) and (b) $p = 0.51$ ($a = 200$ nm and $d = 150$ nm), recorded at two different wave vectors along ΓX (anti-Stokes side) and ΓJ (Stokes side) in the reciprocal lattice. The solid lines indicate the contribution of individual modes, while their superposition is denoted by the solid red line.

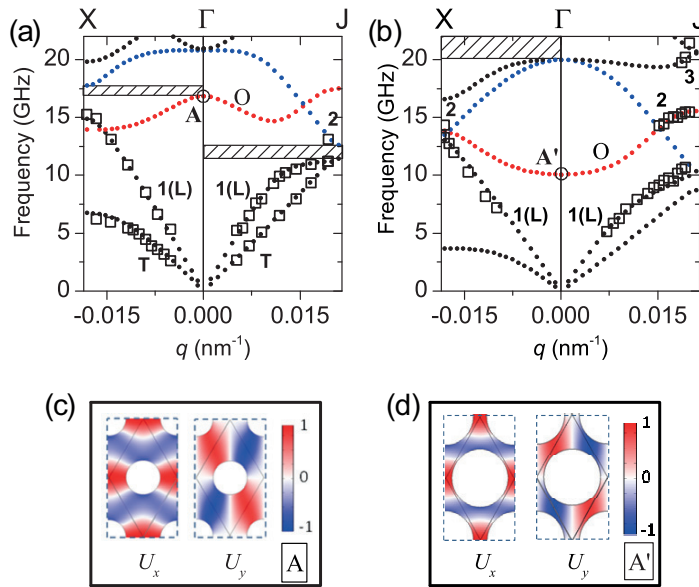


Figure 3. (a), (b) Dispersion relations for the two APA films along ΓX and ΓJ for both longitudinal (L) and transverse (T) phonon propagation, and the hatched regions indicate partial bandgaps. (c), (d) The displacement field distribution (U_x and U_y polarizations) at points A ($q = 0$ nm $^{-1}$, $f = 15.2$ GHz, $p = 0.23$) and A' ($q = 0$ nm $^{-1}$, $f = 10$ GHz, $p = 0.51$).

and (b). Peak **1** is broader and red shifted compared to the polarized spectrum of the single crystalline α -Al₂O₃ known as sapphire (figure S1(a), supplementary data available from stacks.iop.org/NJP/14/113032/mmedia); the longitudinal sound velocity of the latter assumes $c_{L,Al_2O_3} = 11\,320$ m s $^{-1}$, while its shear sound velocities are $c_{T1,Al_2O_3} = 5850$ m s $^{-1}$ and $c_{T2,Al_2O_3} = 6870$ m s $^{-1}$ (figure S1(b)). The acoustic phonon (**1**) at long wavelengths (low q 's) in the two APAs with air cylinders, yields the longitudinal sound velocity $c_L = 5860 \pm 70$ m s $^{-1}$

($p = 0.23$) and $4540 \pm 60 \text{ m s}^{-1}$ ($p = 0.51$), which are much lower than in sapphire. The shear sound velocity was obtained only for the lower porosity APA, for which the depolarized BLS could be recorded; at $p = 0.23$, $c_T = 3110 \pm 40 \text{ m s}^{-1}$ is clearly lower than both $c_{t, \text{Al}_2\text{O}_3}$ in sapphire. Thus the modified structure of Al_2O_3 in the APAs precludes the use of the sapphire elastic constants as the input parameters in the band structure calculations as explained in the next paragraph. It is interesting to note that these c_L , and c_T fall on the same $c_L(p)$ curve obtained for four polydomain APAs [36] with porosities between 11 and 65% (figure S2, supplementary data available from stacks.iop.org/NJP/14/113032/mmedia). In addition to the effective medium acoustic phonon (1), the BLS spectra of APAs displays two additional peaks (modes (2) and (3)) at higher frequencies than mode (1).

In order to provide physical insights into the elastic excitations in APAs with air cylinders, identification of the observed modes in figures 3(a) and (b) is a prerequisite. We have therefore calculated dispersion relations in the APAs with air cylinders along the two selected high-symmetry directions using the FDTD method. The choice of the elastic constants and density for the two components (APA scaffold and filling material) of the nanocomposite is crucial for the FDTD band structure calculations. For the APA scaffold, the values $c_{L-\text{APA}} = 6640 \text{ m s}^{-1}$ and $c_{T-\text{APA}} = 3720 \text{ m s}^{-1}$ are obtained from the corresponding $c_L(p)$ and $c_T(p)$ in figure S2 via extrapolation to zero porosity utilizing their representation by equation (S1) [40]. We found, however, that these sound velocities at $p = 0$ cannot describe well the effective medium mode (1) because of the anticipated morphological modification of APA upon introduction of nanopores. Instead a very good representation was achieved by $c_{L-\text{APA}} = 7300 \text{ m s}^{-1}$ and $c_{T-\text{APA}} = 4300 \text{ m s}^{-1}$, for the APA scaffold with a density of $\rho = 3700 \text{ kg m}^{-3}$. Noticeably, both sound velocities assume higher values than those obtained by extrapolation to zero porosity (figure S2). Lower extrapolated velocities at $p = 0$ are anticipated if we consider the morphology and substructure of APA. An anodically formed Al_2O_3 film is described as an amorphous structure with significant incorporations of water, and density inhomogeneities are expected due to the nonuniform distributions of several alumina minerals in the film. In fact, a reduced density of $2880 \pm 355 \text{ kg m}^{-3}$ relative to sapphire (3980 kg m^{-3}) was revealed in our previous study of APA [37]. Therefore, the softening of the zero porosity sound velocity values can be ascribed to a structural modification of APA due to the fabrication process and the functions $c_L(p)$, $c_T(p)$ should be discontinuous at $p = 0$, since the initiation of nanopores renders the morphology different from porous-free APA. This can also rationalize why $c_{L-\text{APA}}$ and $c_{T-\text{APA}}$ values higher by $\sim 10\%$ are needed for the FDTD calculations in order to capture the frequency of the effective medium mode (1).

The comparison of experimental and theoretical phonon dispersion relations for APA with air cylinders is depicted in figures 3(a) and (b). The first longitudinal propagation mode (1) is bent weakly along ΓX but strongly in the ΓJ direction as opposed to the transverse modes, which correspond to the two lowest branches in figure 3(a). The different behaviors along the two directions can be explained by symmetry reasons, taking into account the interactions of the acoustic branches with the branch denoted (O) in figures 3(a) and (b). The x and y components of the displacement field for the branch (O) at point A implies a symmetric behavior with respect to the x -axis (parallel to the direction ΓJ) and an antisymmetric behavior with respect to the y -axis (parallel to the direction ΓX) as seen in figure 3(c). Hence, for propagation along ΓJ , the branch (O) will couple with the longitudinal acoustic branch possessing the same symmetry but will have no interaction with the transverse acoustic branch which has a different symmetry.

The opposite situation applies along the ΓX direction and, moreover, branch **(O)** can even cross (figure 3(a)) the longitudinal acoustic branch without any interaction. Due to the different dependence on porosity, the locus of branch **(O)** drops more strongly with porosity than the longitudinal mode **(1)**. This behavior is observed only in the present coherent APA structure due to the association of the new branch **(O)** with collective displacements of the APA material between neighboring air cylinders (figures 3(c) and (d)). The FDTD calculations further help to assign the experimentally observed mode **(2)** (figures 2(a) and (b)). Its association with either branch **(O)** or a higher-frequency branch (blue dotted line in figures 3(a) and (b)) depends on both the propagation direction and the porosity. A third weaker mode **(3)** observed along ΓJ at $p = 0.51$, falls at an even higher frequency (~ 20 GHz) branch. The obtained description of all the observed modes is a strong support of their origin and, moreover, justifies the choice of the elastic parameters and density of APA utilized for theoretical calculations. We should, finally, recall that the experimental band diagrams of monodomain (figures 3(a) and (b)) and polydomain (figure 1(a), and figure 3 of [36]) APAs with air cylinders are qualitatively different.

3.2. APA with liquid poly-ethylene oxide cylinders

The BLS spectra of APA nanocomposites change significantly upon infiltration with liquid PEO in figures 4(a)–(d) recorded at the same q 's and temperature (70°C) above the melting temperature of PEO as compared to the spectra of the APA with air cylinders (figures 2(a) and (b)). The longitudinal phonon peaks **(1)** in both the ΓX and ΓJ directions are red shifted relative to the peak **(1)** of the APA with air cylinders and consequently the effective medium becomes softer upon filling the nanopores with PEO. This appears to be counterintuitive for filled APAs in which the acoustic phonons propagate the effective medium, e.g. the APA scaffold and liquid residing in the nanopores. Instead, the effective medium longitudinal phonon in the corresponding APAs with air cylinders propagates predominantly through the APA scaffold [36]. The marked 'PEO_l' peak in figure 4(a) is attributed to the liquid PEO layer on the APA surface and expectedly yields the value of the longitudinal sound velocity $c_{L\text{-PEO}l}$ ($= 1480 \text{ m s}^{-1}$ at 70°C) in liquid PEO.

Other characteristic features observed in APA with liquid PEO cylinders are the two higher-frequency modes, **(2)** and **(3)**, representing phonons propagating in higher propagation bands than the acoustic mode **(1)**. The intensities of these modes, relative to the longitudinal mode **(1)**, appeared to depend on the probed directions in the APA with liquid PEO cylinders as seen in the anti-Stokes and Stokes panels of figure 4 for the two examined porosities. The nature of the different elastic excitations in the APA with liquid PEO cylinders is manifested in the dispersion $\omega(\mathbf{q})$ and in the spatial distribution of the computed displacement fields of the contributing modes displayed in figure 5. For the FDTD calculations, in addition to the density and sound velocity values of the APA scaffold used for the FDTD calculations, we utilized a density of 1045 kg m^{-3} and a longitudinal sound velocity of liquid PEO (inside the nanopores) of 1300 m s^{-1} , which is noticeably lower than the experimental $c_{L\text{-PEO}l}$ ($= 1480 \text{ m s}^{-1}$ for the bulk PEO). This low value of the 'effective' sound velocity of PEO, however, is needed since it sensitively determines the experimental frequency of the flat mode **(R)** (green dots in figures 5(a) and (b)).

Surprisingly, the acoustic branches **(1)** in the present APA with PEO cylinders become flat at the same frequency, regardless of the propagation direction as seen in figure 5(a) (at ~ 7.5 GHz for $p = 0.23$) and figure 5(b) (at ~ 5 GHz for $p = 0.51$). These frequency values scale with

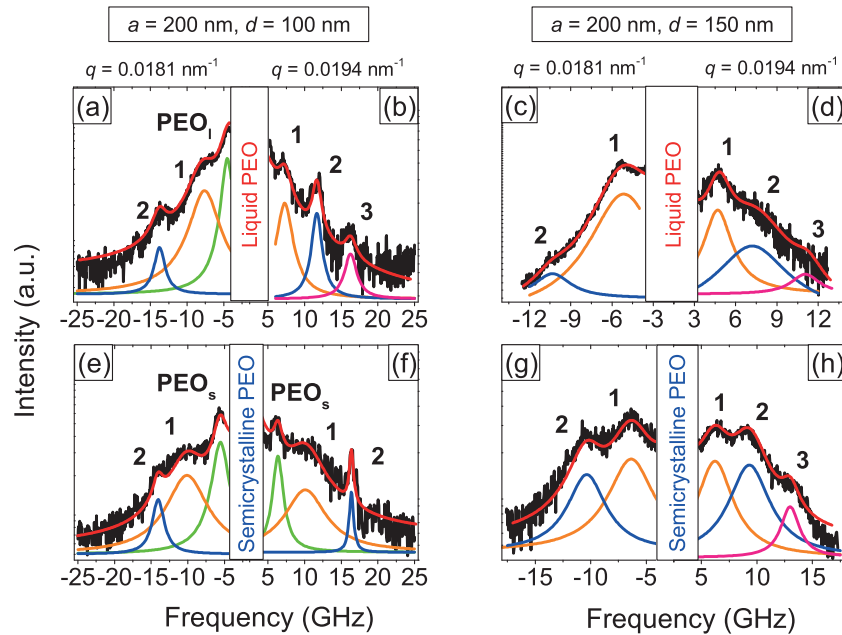


Figure 4. (a)–(h) Polarized BLS spectra of APA of PEO (liquid and semi-crystalline) cylinders with the same porosities of the APAs (figure 2) recorded at two different wave vectors along ΓX (anti-Stokes side) and ΓJ (Stokes side). The solid lines indicate the contribution of the individual modes, while their superposition is denoted by the solid red line. The peak marked ‘PEO_{l,s}’ is associated with either the fluid or the solid PEO film on the surface of the APA membrane.

the reciprocal diameter of the nanopores, suggesting localized modes of the liquid cylinders. Remarkably, the band diagrams are distinctly different from the corresponding diagrams of APAs with air cylinders (figures 3(a) and (b)) while they resemble those of polydomain APAs with liquid cylinders [36]. Infiltrated APA ($p = 0.23$) with another viscous liquid (polydimethylsiloxane (PDMS)) leads to a similar dispersion diagram (figure S3, supplementary data available from stacks.iop.org/NJP/14/113032/mmedia) with a flat band (**R**) at the (lower) frequency ~ 5 GHz following the trend of the (lower) c_{L-PDMS} relative to c_{L-PEOI} at a constant pore diameter ($d = 100$ nm). This affirms the origin of (**R**) with a scaling $f_R \sim c_{L-1}/d$, where c_{L-1} is the longitudinal sound phase velocity of the liquid residing in the nanopores (see also below). Nevertheless, the softness of the liquid cylinders (either PEO or PDMS) is an unexpected finding which can be vaguely rationalized by a structural modification of the liquid phase under confinement, particularly in the proximity of the APA wall. In this context, it was reported in [41] for PDMS that cylindrical confinement can promote a self-induced layered structure.

This generic feature of liquid inclusions is in accord with the localized resonance nature of the flat mode (**R**) inside the nanopores with liquid PEO, as nicely mapped in the displacement field (figure S4(a)) at Γ (point B in figure 5(a)). The trend of the dispersion diagrams can be attributed to the hybridization of the propagating acoustic modes in the background with a localized mode in the nanopores [5, 7–9]. The low-frequency region of the dispersion diagram (below the frequency of band (**R**)) for the APA with liquid PEO cylinders is direction

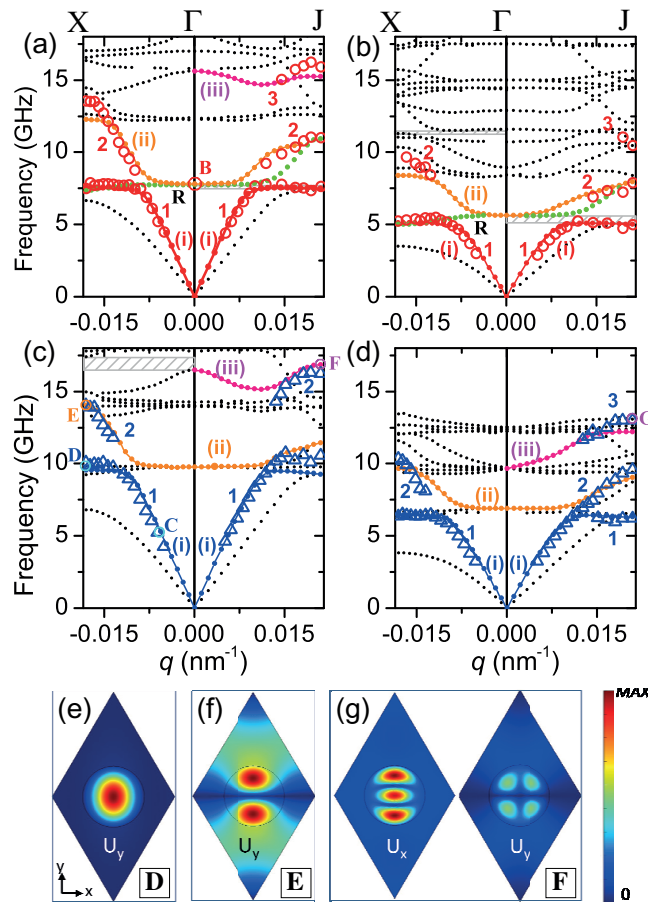


Figure 5. (a)–(d) Dispersion relations in APA of PEO (liquid or semicrystalline) cylinders along the ΓX and ΓJ directions for $p = 0.23$ and 0.51 porosity. The black dotted lines represent theoretical dispersion relations, while the red circles and blue triangles represent experimental dispersion relations. The blue, orange, green and magenta dots represent branches which are representative of the observed modes. The hatched regions indicate partial bandgaps. All dispersion relations represent the longitudinal mode. (e)–(g) Components of the displacement field at different points of the dispersion diagram (c): longitudinal component at 9.83 GHz (e) and 14.05 GHz (f) with increasing proximity to the point X of the BZ, and the two components (longitudinal (U_x) and transverse (U_y)) near the point J of the BZ at 16.85 GHz.

independent (branch (i) in figures 5(a) and (b)). This direction invariance is in clear contrast to their air-cylinder analogues (figures 3(a) and (b)) but in harmony with infiltrated polydomain APAs. It is the interaction between mode (1) and the characteristic band (R) that erases the signature of the structure periodicity when the air cylinders are filled with fluids and renders the low-frequency band diagrams robust; at frequencies above that of (R) the symmetry effect is recovered. The differences at the high-frequency region above the flat band (R) relate to the coherence of the APA structure as discussed below for the APA with PEO cylinders. We recall that a slower (by about 10%) sound velocity than the bulk PEO has to be used in order

to capture theoretically the experimental frequency of mode **(R)**. Assuming hard confinement of the liquid cylinders, the first resonance frequency should occur at $f_R = \kappa c_{L-1}/(\pi d)$, where $\kappa = 1.84$ is the first solution of $j_1'(x) = 0$ with $j_1(x)$ being the Bessel function of the order of 1. The experimental **(R)** for the two diameters leads to $c_{L-PEOI} \sim 1300 \text{ m s}^{-1}$, which is the value used in the FDTD calculations. The fact that c_{L-1} (1 = PEO, PDMS) becomes softer compared to the bulk liquids might indicate different packings inside the APA nanopores.

3.3. APA with solid cylinders

For APA with solid PEO cylinders at 20 °C, the peak denoted as ‘PEO_s’ (figures 4(e) and (f)) expectedly appears at higher frequency than the ‘PEO_l’ peak for the APA with liquid PEO cylinders (figure 4(a)) due to the higher longitudinal sound velocity in bulk crystalline PEO ($c_{L-PEOs} = 3050 \text{ m s}^{-1}$) than that of c_{L-PEOI} . Unexpectedly, however, the ‘PEO_s’ peak yields a much lower $c_{L-PEO*} = 2030 \text{ m s}^{-1}$ than c_{L-PEOs} . A meaningful account for this observation is probably a modified semicrystalline solid PEO* layer on top of the APA. In theory, the flat modes **(R)** ($\sim 10 \text{ GHz}$ for $p = 0.23$ and $\sim 8 \text{ GHz}$ for $p = 0.51$) as well as the longitudinal mode **(1)** for both porosities in figures 5(c) and (d) are captured using $c_{L-PEO*} = 1660 \pm 50 \text{ m s}^{-1}$, $c_{T-PEO*} = 800 \text{ m s}^{-1}$ and $\rho = 1045 \text{ kg m}^{-3}$. With regard to these low values, we first note that the shear velocity is lower than a typical value for glassy polymers ($\sim 1400 \text{ m s}^{-1}$), but due to concurrently low longitudinal sound velocity the Poisson ratio (~ 0.34) assumes a value typical of polymeric glasses. For the low c_{L-PEO*} , a possible explanation is the suppression of crystallinity of PEO within the one-dimensional hard confinement of APA. Crystallization kinetics of PEO are substantially hampered under 2D hard confinement in block copolymers [42] as well as in droplets [43]. Since the nucleation process of PEO in these confinements can be ascribed to homogeneous nucleation, crystallization of PEO occurs below $T \leq 0 \text{ °C}$. The low value of c_{L-PEO*} suggests a hindered PEO crystallization in the APA nanopores and the effective medium theory [44] estimates the crystallinity of 60% on top of the APA and 25% inside its nanopores.

With regard to the assignment of the high-frequency modes **(2)** and **(3)** in APA of PEO (liquid or semicrystalline) cylinders, an inspection of the experimental spectra of figure 4 and the dispersion diagrams in figure 5 reveals qualitative differences for the wave propagation along ΓX and ΓJ .

Along ΓX the same modes **(1)** and **(2)** are observed for both porosities.

- Mode **(1)**, linking to branch **(i)**, originates from the effective medium phonon with longitudinal polarization U_y (figure S4(b) along ΓX , available from stacks.iop.org/NJP/14/113032/mmedia) belonging to point C ($q = 0.00573 \text{ nm}^{-1}$; $f = 5.3 \text{ GHz}$; as indicated in figure 5(c)) at low q 's and becomes localized in the PEO cylinders at high q 's approaching the BZ at X as seen in the displacement field distribution of figure 5(e) at point D ($q = 0.0181 \text{ nm}^{-1}$; $f = 9.83 \text{ GHz}$) for 23% porosity.
- Mode **(2)** relates to branch **(ii)**. Based on the displacement field of figure 5(f) at the edge of the BZ ($q = 0.0181 \text{ nm}^{-1}$; $f = 14.05 \text{ GHz}$; indicated as E in figure 5(c)), mode **(2)** has predominantly longitudinal polarization U_y , is mainly localized in the filled nanopores and associated with more oscillations in U_y than mode **(1)** at the same point of the BZ. The pattern evolution from figures 5(e) to (f) can rationalize the lower scattering intensity of mode **(2)** relative to mode **(1)** as revealed from the comparison of the spectra in figures 4(e) and (g) for both porosities.

Along ΓJ , the BLS spectra of figures 4(f) and (h) for the APA with semicrystalline PEO cylinders reveal a porosity-dependent phononic behavior.

- For $p = 0.23$, the frequency separation between modes (2) and (1) is larger as compared with that along ΓX , and mode (2) now falls onto a new branch (iii) (figures 5(c) and (d)). Based on the displacement field distribution of figure 5(g) at point F ($q = 0.021 \text{ nm}^{-1}$; $f = 16.85 \text{ GHz}$), mode (2) has a mixed polarization and displays oscillations. Hence, due to these characteristics, it is much weaker than mode (1) (figure 4(f)). The different assignment of mode (2), i.e. to (iii) and not to (ii), is also corroborated by the much broader line shape of mode (1) in figure 4(f); mode (1) now bears both contributions from branches (i) and (ii) owing to their proximity (figure 5(c) along ΓJ). In the same context, it is worth mentioning that as the separation between modes (1) and (2) along the same direction is increased, e.g., by melting PEO (figure 5(b)), the resolved mode (2) (figure 5(b)) is then assigned to branch (ii). The appearance of a very weak mode (3) might be assigned to branch (iii) as seen in figure 5(a). The same situation occurs for the APA with semicrystalline PEO cylinders at 51% porosity.
- For $p = 0.51$, branches (i) and (ii) are indeed well apart (at high q 's along ΓJ) and now the observed mode (2) is again assigned to branch (ii) due to its sufficiently large separation from the frequency of mode (1) (figure 4(h)). Based on the displacement field distribution, branch (ii) is predominantly localized in PEO cylinders. Therefore, mode (2) has now comparable intensity to mode (1) with the appearance of the higher-frequency mode (3) (figure 4(h)). The latter mode falls on branch (iii) which has a mixed polarization as the same branch along the same direction for $p = 0.23$; the high-frequency mode (3) displays more oscillations in its displacement field (figure S4(c), supplementary data available from stacks.iop.org/NJP/14/113032/mmedia) belonging to point G ($q = 0.021 \text{ nm}^{-1}$; $f = 13 \text{ GHz}$), thus causing a reduced scattering contribution to the BLS spectrum. It is worth mentioning that filling the nanopores nullifies the direction dependence of low-frequency branch (i) in the APA with air cylinders, while the higher-frequency branches (ii) and (iii) are distinct along the two symmetry directions.

For the two phononic crystals, there is only a partial bandgap along either the ΓJ or ΓX direction. Moreover, theoretical dispersion relations confirmed a complete bandgap in APA of poly(dimethyl siloxane) (PDMS; $M_w = 1350 \text{ g mol}^{-1}$) cylinders. However, a complete bandgap with a central frequency of $f_{\text{gap}} = 5 \text{ GHz}$ and with a width of $\Delta f = 0.12 \text{ GHz}$ corresponding to a $\Delta f/f_{\text{gap}}$ of 2.4% is so narrow that it is difficult to resolve the split characteristic of the BLS spectrum experimentally (figure S3). In general, hexagonal lattice air or filled with soft materials is not a good candidate to open large complete gaps.

4. Conclusions

In the present experimental and theoretical paper, we have verified the complete dispersion relations in 2D hypersonic phononic crystals composed of a triangular array of air and PEO cylinders in APA and elucidated the different phononic nature altering the wave propagation phenomena. Both experimental and theoretical observations underline the fundamental physical picture emerging for hypersonic phononic crystals. For the particular geometry and phononic properties investigated here, only the partial bandgaps are formed along either the ΓX or ΓJ direction. The formation of a complete bandgap can be further explored by varying the

geometrical properties such as honeycomb and square structures [45–47]. This work can provide a comprehensive foundation for controlling the flow of the elastic energy, showing the linkage between the symmetry and propagation phenomena or filling materials and propagation phenomena.

Acknowledgments

This work was partially supported by the Ministry of Higher Education and Research, the Nord-Pas de Calais Regional Council and the Fonds Européen de Développement Régional (FEDER) through the contract de Projets Etat Region CPER (2007-2013). GF acknowledges the GSRT of Greece (ARISTEIA Program) and the University of Lille for a honor professionship (2012).

References

- [1] Gorishnyy T, Maldovan M, Ullal C and Thomas E 2005 *Phys. World* **18** 24–9
- [2] Wang L and Li B 2008 *Phys. World* **27** 27–9
- [3] Kushwaha M S, Halevi P, Dobrzynski L and Djafari-Rouhani B 1993 *Phys. Rev. Lett.* **71** 2022–5
- [4] Sigalas M and Economou E N 1993 *Solid State Commun.* **86** 141–3
- [5] Liu Z Y, Zhang X X, Mao Y W, Zhu Y Y, Yang Z Y, Chan C T and Sheng P 2000 *Science* **289** 1734
- [6] Psarobas I E, Modinos A, Sainidou R and Stefanou N 2002 *Phys. Rev. B* **65** 064307
- [7] Still T, Cheng W, Retsch M, Sainidou R, Wang J, Jonas U, Stefanou N and Fytas G 2008 *Phys. Rev. Lett.* **100** 194301
- [8] Leroy V, Bretagne A, Fink M, Willaime H, Tabeling P and Tourin A 2009 *Appl. Phys. Lett.* **95** 171904
- [9] Cowan M L, Page J H and Sheng P 2011 *Phys. Rev. B* **84** 094305
- [10] Lu M H *et al* 2007 *Nature Mater.* **6** 744
- [11] Sukhovich A, Merheb B, Muralidharan K, Vasseur J O, Pennec Y, Deymier P A and Page J H 2009 *Phys. Rev. Lett.* **102** 154301
- [12] Fang N, Xi D J, Xu J Y, Ambati M, Srituravanich W, Sun C and Zhang X 2006 *Nature Mater.* **5** 452
- [13] Cummer S A, Popa B I, Schurig D, Smith D R, Pendry J, Rahm M and Starr A 2008 *Phys. Rev. Lett.* **100** 024301
- [14] Cheng J C, Liang B, Guo X S, Tu J and Zhang D 2010 *Nature Mater.* **9** 989
- [15] Li X F, Ni X, Feng L A, Lu M H, He C and Chen Y F 2011 *Phys. Rev. Lett.* **106** 084301
- [16] Martinezsala R, Sancho J, Sanchez J V, Gomez V, Llinares J and Meseguer F 1995 *Nature* **378** 241
- [17] Vasseur J O, Deymier P A, Chenni B, Djafari-Rouhani B, Dobrzynski L and Prevost D 2001 *Phys. Rev. Lett.* **86** 3012–5
- [18] Cheng W, Wang J J, Jonas U, Fytas G and Stefanou N 2006 *Nature Mater.* **5** 830
- [19] Gorishnyy T, Jang J H, Koh C and Thomas E L 2007 *Appl. Phys. Lett.* **91** 121915
- [20] Jang J H, Koh C Y, Bertoldi K, Boyce M C and Thomas E L 2009 *Nano Lett.* **9** 2113
- [21] Parsons L C and Andrews G T 2009 *Appl. Phys. Lett.* **95** 241909
- [22] Gomopoulos N, Maschke D, Koh C Y, Thomas E L, Tremel W, Butt H J and Fytas G 2010 *Nano Lett.* **10** 980–4
- [23] Salasyuk A S *et al* 2010 *Nano Lett.* **10** 1319
- [24] Walker P M, Sharp J S, Akimov A V and Kent A J 2010 *Appl. Phys. Lett.* **97** 073106
- [25] Aliev G N, Goller B, Kovalev D and Snow P A 2010 *Appl. Phys. Lett.* **96** 124101
- [26] Still T, Gantzounis G, Kiefer D, Hellmann G, Sainidou R, Fytas G and Stefanou N 2011 *Phys. Rev. Lett.* **106** 175505
- [27] Maldovan M and Thomas E L 2006 *Appl. Phys. Lett.* **88** 251907
- [28] Eichenfield M, Chan J, Camacho R M, Vahala K J and Painter O 2009 *Nature* **462** 78

- [29] Psarobas I E, Papanikolaou N, Stefanou N, Djafari-Rouhani B, Bonello B and Laude V 2010 *Phys. Rev. B* **82** 174303
- [30] Pernot G *et al* 2010 *Nature Mater.* **9** 491
- [31] Moctezuma-Enriquez D, Rodriguez-Viveros Y J, Manzanares-Martinez M B, Castro-Garay P, Urrutia-Banuelos E and Manzanares-Martinez J 2011 *Appl. Phys. Lett.* **99** 171901
- [32] Grimm S, Giesa R, Sklarek K, Langner A, Gosele U, Schmidt H W and Steinhart M 2008 *Nano Lett.* **8** 1954
- [33] Masuda H, Ohya M, Asoh H, Nakao M, Nohtomi M and Tamamura T 1999 *Japan. J. Appl. Phys.* **2** **38** L1403
- [34] Masuda H, Ohya M, Nishio K, Asoh H, Nakao M, Nohtomi M, Yokoo A and Tamamura T 2000 *Japan. J. Appl. Phys.* **2** **39** L1039
- [35] Dainese P, Russell P S J, Joly N, Knight J C, Wiederhecker G S, Fragnito H L, Laude V and Khelif A 2006 *Nature Phys.* **2** 388
- [36] Sato A, Knoll W, Pennec Y, Djafari-Rouhani B, Fytas G and Steinhart M 2009 *J. Chem. Phys.* **130** 111102
- [37] Sato A, Pennec Y, Shingne N, Thum-Albrecht T, Knoll W, Steinhart M, Djafari-Rouhani B and Fytas G 2010 *ACS Nano* **4** 3471
- [38] Mechri C, Ruello P and Gusev V 2012 *New J. Phys.* **14** 023048
- [39] Masuda H, Yamada M, Matsumoto F, Yokoyama S, Mashiko S, Nakao M and Nishio K 2006 *Adv. Mater.* **18** 213
- [40] Aliev G N, Goller B and Snow P A 2011 *J. Appl. Phys.* **110** 043534
- [41] Jagadeesh B, Demco D E and Blumich B 2004 *Chem. Phys. Lett.* **393** 416–20
- [42] Huang P *et al* 2006 *Polymer* **47** 5457
- [43] Massa M V and Dalnoki-Veress K 2004 *Phys. Rev. Lett.* **92** 255509
- [44] Coste C, Laroche C and Fauve S 1992 *Phys. Rev. Lett.* **69** 765
- [45] Vasseur J O, Djafari-Rouhani B, Dobrzynski L, Kushwaha M S and Halevi P 1994 *J. Phys.: Condens. Matter* **6** 8759
- [46] Vasseur J O, Djafari-Rouhani B, Dobrzynski L and Deymier P A 1997 *J. Phys.: Condens. Matter* **9** 7327
- [47] Masuda H, Asoh H, Watanabe M, Nishio K, Nakao M and Tamamura T 2001 *Adv. Mater.* **13** 189